ACSNANO
www.acsnano.org
ARTICLE

Ultrafast Charge Transfer and Enhanced Absorption in MoS_2–Organic van der Waals Heterojunctions Using Plasmonic Metasurfaces

Christopher E. Petoukhoff,*[,†,‡] M. Bala Murali Krishna,[‡] Damien Voiry,[†,⊥] Ibrahim Bozkurt,[†] Skylar Deckoff-Jones,[‡] Manish Chhowalla,[†] Deirdre M. O'Carroll,[†,§] and Keshav M. Dani[‡]

[†]Department of Materials Science and Engineering, Rutgers University, 607 Taylor Road, Piscataway, New Jersey 08854, United States

[‡]Femtosecond Spectroscopy Unit, Okinawa Institute of Science and Technology Graduate University, 1919-1 Tancha, Onna-son, Okinawa 904-0495, Japan

[§]Department of Chemistry and Chemical Biology, Rutgers University, 610 Taylor Road, Piscataway, New Jersey 08854, United States

Supporting Information

ABSTRACT: Hybrid organic–inorganic heterostructures are attracting tremendous attention for optoelectronic applications due to their low-cost processing and high performance in devices. In particular, van der Waals p–n heterojunctions formed between inorganic two-dimensional (2D) materials and organic semiconductors are of interest due to the quantum confinement effects of 2D materials and the synthetic control of the physical properties of organic semiconductors, enabling a high degree of tunable optoelectronic properties for the heterostructure. However, for photovoltaic applications, hybrid 2D–organic heterojunctions have demonstrated low power conversion efficiencies due to the limited absorption from constraints on the physical thickness of each layer. Here, we investigate the ultrafast charge transfer dynamics between an organic polymer:fullerene blend and 2D n-type MoS_2 using transient pump–probe reflectometry. We employ plasmonic metasurfaces to enhance the absorption and charge photogeneration within the physically thin hybrid MoS_2–organic heterojunction. For the hybrid MoS_2–organic heterojunction in the presence of the plasmonic metasurface, the charge generation within the polymer is enhanced 6-fold, and the total active layer absorption bandwidth is increased by 90 nm relative to the polymer:fullerene blend alone. We demonstrate that MoS_2–organic heterojunctions can serve as hybrid solar cells, and their efficiencies can be improved using plasmonic metasurfaces.

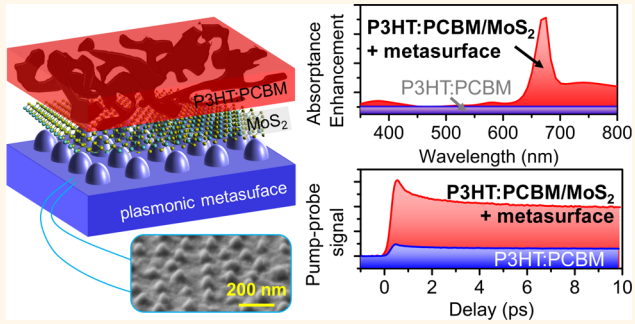

KEYWORDS: *two-dimensional materials, hybrid organic–inorganic heterostructures, plasmonic metasurfaces, ultrafast pump–probe dynamics, charge transfer, solar energy*

A great deal of interest has been generated recently for thin-film photovoltaics because of the reduced material waste, low-cost manufacturing, and flexible, lightweight devices associated with this next-generation solar energy technology.[1] Emerging thin-film photovoltaics have relied heavily on hybrid active layers composed of organic–inorganic heterojunctions, which tend to be less expensive and well-suited to more versatile applications than conventional Si-based photovoltaics.[2−9] For example, hybrid organic–inorganic perovskites have led to the fastest growth in their power conversion efficiencies (PCEs) since 2009,[10] reaching values of more than 20% by 2015.[11] Additionally, heterojunctions have been formed between organic dyes or polymers with either quantum dots,[12−14] metal oxide nanoparticles,[15,16] or mesoporous TiO_2 (*i.e.*, dye-sensitized solar cells).[8,9,17−20] These types of hybrid organic–inorganic materials combine the properties of organic semiconductors (*e.g.*, solution-based processing,[21,22] large absorption cross sections,[23,24] synthetic tunability,[25,26] and mechanical flexibility[27]) with those of traditional inorganic semiconductors (*e.g.*, large carrier mobilities, stability) to create heterostructures with advanced functionalities. More recently, p–n van der Waals heterojunctions have been fabricated using inorganic two-dimensional (2D) materials combined with organic semiconductors.[28−31] Both 2D and organic semiconductors lack dangling bonds at

Received: May 24, 2016
Accepted: November 8, 2016
Published: November 8, 2016

DOI: 10.1021/acsnano.6b03414
ACS Nano XXXX, XXX, XXX–XXX

their surfaces, which allow them to interact *via* van der Waals forces, enabling ideal interfaces between the two materials.[29] Because of the extensive developing library of 2D materials,[32−34] including graphene, hexagonal boron nitride, transition metal dichalcogenides, and layered oxides, coupled with the synthetic tunability of organic semiconductors, van der Waals heterostructures formed between 2D materials with organic semiconductors allows for nearly limitless tailoring of the resulting properties of the hybrid material. MoS_2 is particularly interesting as the n-type material in hybrid solar cells due to its direct band gap in the monolayer,[35−37] high absorption coefficient,[36,38−40] and tunable band gap for multilayer thin films.[36,41−44] For example, single-crystal 2D MoS_2 has been employed as the n-type material in heterojunctions with few-layer molecular crystals[28,30] and small-molecule thin films,[29,31] and liquid-phase exfoliated MoS_2 flakes have been used in heterojunctions with conjugated polymer thin films.[42] In these studies, rectification ratios of up to 10^5 have been observed,[28,30] and the photovoltaic effect has been demonstrated, suggesting charge transfer from the p-type organic material to the n-type MoS_2. However, there have been limited studies exploring the charge transfer across the interface between 2D and organic semiconductors.

Organic−2D p−n heterojunctions that have exhibited photovoltaic responses have, to-date, had extremely low power conversion efficiencies (less than 1%).[28,29,31] One major limitation for the low PCE is from the limited thickness of the active layer: in order to exploit the quantum confinement effects of the 2D material, the material should be either a single or a few layers in thickness. Similarly, organic semiconductors, which have low carrier mobilities, should be kept physically thin to minimize charge recombination in the active layer.[45−47] However, keeping the active layer materials physically thin prevents them from being optically thick. Plasmonic nanostructures and metasurfaces have been shown to increase absorption in ultrathin organic films[48−54] and 2D semiconductors[55−64] due to their large scattering cross sections and local electromagnetic field enhancements near the surface of the metallic nanostructure. In addition, plasmonic metasurfaces (*i.e.*, nanostructured metallic films) can couple incident light into surface plasmon polaritons (SPPs), which propagate along the interface between the metasurface and the active layer coating. This allows the unabsorbed incident light to be redirected into in-plane guided modes that can travel several orders of magnitude longer than the physical thickness of the active layer.[65−67] This can allow the ultrathin active layers to become optically thick while maintaining a physically thin film to preserve the monolayer properties of the 2D material and minimize charge carrier recombination in the organic layer, thereby potentially leading to an improved PCE.

Here, we combine a hybrid MoS_2−organic heterojunction active layer with a disordered plasmonic metasurface in order to increase the absorption within the physically thin hybrid active layer. We investigated a hybrid active layer composed of poly(3-hexylthiophene) (P3HT) blended with phenyl-C_{61}-butyric acid methyl ester (PCBM) as the organic component interfaced with n-type MoS_2 as the inorganic 2D material. We performed absorption measurements in the visible to understand the influence of the plasmonic metasurface on the efficiency of carrier generation in the P3HT:PCBM/MoS_2 heterojunction above the band gap. Using time-resolved visible pump−NIR probe reflectometry, we studied the dynamics of the polaron and exciton states that form after photoexcitation. We observed a 6-fold enhancement in the P3HT polaron signal and a 90 nm increase in the absorption bandwidth for the hybrid MoS_2−organic active layer in the presence of the plasmonic metasurface. We show that the 6-fold enhancement in the P3HT polaron signal arose from a combination of increased absorption in both the P3HT:PCBM and MoS_2 layers with ultrafast hole transfer from MoS_2 to P3HT. Thus, we demonstrate that through the combined synergistic effect of hybrid 2D−organic heterojunctions and plasmonic metasurfaces one can potentially enhance efficiencies of thin-film solar cells.

RESULTS AND DISCUSSION

To study the influence of the plasmonic metasurfaces on hybrid MoS_2−organic active layers, first, we prepared large-area plasmonic metasurfaces composed of disordered Ag nanoparticle arrays on Ag films (AgNPA/Ag) by employing the nanotemplating method (Figure 1a,c).[50,68,69] Single-layer 2H-phase MoS_2 thin films (Figure 1b) were grown on SiO_2/Si wafers by chemical vapor deposition (CVD) over an area larger than 1 mm^2 (see Methods and Supporting Information Figures S1 and S2). The MoS_2 films were then transferred to either planar Ag surfaces or plasmonic metasurfaces (Figure 1d−f). Raman spectra obtained from the transferred MoS_2 (Figure 1g) showed the two dominant vibrational modes: the in-plane mode, E^1_{2g}, and the out-of-plane mode, A_{1g}. The frequency difference between the two modes (Δ) was ∼20 cm^{-1}, which confirmed the single-layer nature of the films[70] as measured using atomic force microscopy (Supporting Information Figure S1). We note that the MoS_2 film was uniform on the planar Ag substrate (Supporting Information Figure S3), whereas the MoS_2 on the plasmonic metasurface partially conformed to the surface of the Ag nanoparticles (AgNPs), as seen by the dark patches in the SEM image (Figure 1d). The P3HT:PCBM active layer coating was then deposited by spin-coating to achieve a thickness of 79.3 ± 7.2 nm. Bright- and dark-field images of P3HT:PCBM/MoS_2 on the plasmonic metasurface show the large-area coverage of the MoS_2 films and the plasmonic metasurface (Figure 1e,f).

To study the charge photogeneration and transfer in the hybrid MoS_2−organic active layer, with and without the plasmonic metasurface, we employed two-color transient pump−probe reflection measurements (Figure 2) using a 1 kHz, 800 nm, 70 fs amplified laser. We used pump wavelengths of either 400 nm, by frequency doubling a portion of the fundamental 800 nm laser output, or 800 nm itself. The remainder of the laser power was directed to an optical parametric amplifier (OPA) to generate probe wavelengths of either 1000 nm (Figure 2a) or 1150 nm (Figure 2b), thereby allowing the investigation of polaron and exciton dynamics within the organic polymer, P3HT, as explained below. The transient pump−probe reflection signal ($\Delta R/R$) at 1000 nm originated from the populations of both P3HT excitons (*i.e.*, bound electron−hole pairs) and polarons (*i.e.*, free charges within the polarizable organic polymer).[71−74] For the 1000 nm probe wavelength, the $\Delta R/R$ signal was larger for the hybrid P3HT:PCBM/MoS_2 active layer relative to P3HT:PCBM alone, demonstrating that MoS_2 contributed to the polaron or exciton population within P3HT:PCBM (note that the $\Delta R/R$ signal was zero for MoS_2 alone, see Supporting Information Figure S4). The $\Delta R/R$ signal at 1150 nm (Figure 2b), which originated from the population of P3HT excitons alone,[71,73,74] showed a negligible increase for the hybrid P3HT:PCBM/

DOI: 10.1021/acsnano.6b03414
ACS Nano XXXX, XXX, XXX−XXX

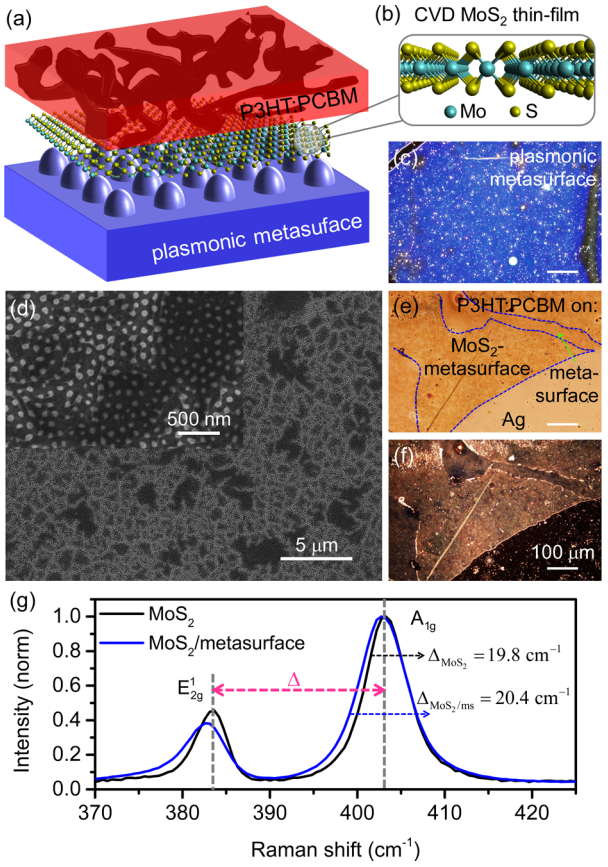

Figure 1. (a) Schematic of the hybrid P3HT:PCBM/MoS_2 heterojunction on a plasmonic metasurface. (b) Cross-sectional schematic of monolayer MoS_2. (c) True-color dark-field image of a Ag nanoparticle array on a Ag film plasmonic metasurface; scale bar value shown in (f). (d) SEM image of MoS_2 on the plasmonic metasurface prior to application of P3HT:PCBM. Inset is a magnified view of the MoS_2-coated metasurface. (e, f) Optical images for P3HT:PCBM/MoS_2 on a plasmonic metasurface. The bright-field image (e) is labeled with different regions near the edges of the MoS_2 film; the dark-field image (f) was acquired from the same area and helped to identify the different regions. Bright- and dark-field images are on the same scale (value shown in (f)). (g) Raman spectra of CVD-grown MoS_2 thin films after being transferred onto the Ag and metasurface substrates. The two dominant vibrational modes are labeled.

MoS_2 active layer, which proves that the increased $\Delta R/R$ signal at 1000 nm arose from an increased P3HT polaron population. This suggests that hole transfer occurred from the MoS_2 to the P3HT. Because the $\Delta R/R$ signal was enhanced from the earliest, instrument-limited time scales, this hole transfer process was determined to occur within 100 fs.

The hybrid P3HT:PCBM/MoS_2 active layer employing the plasmonic metasurface exhibited more than a 6-fold enhancement in the $\Delta R/R$ signal at 1000 nm relative to P3HT:PCBM alone for both 400 nm (Figure 2a) and 800 nm excitation (Supporting Information Figure S5). Although the plasmonic metasurface also led to enhancement of the $\Delta R/R$ signal in the pure organic active layer (P3HT:PCBM), the enhancement was significantly larger for the hybrid MoS_2–organic active layer. The small increases observed in the $\Delta R/R$ signal at 1150 nm in the presence of the plasmonic metasurface arose from collective electric field enhancements of the metasurface[50] and increased light scattering from MoS_2 (see Supporting Information Figure S6); we note that interference effects from the addition of the monolayer MoS_2 film between P3HT:PCBM and Ag did not significantly impact the $\Delta R/R$ signals (see Supporting Information Figure S7). However, the $\Delta R/R$ signal at 1000 nm exhibited a much larger increase, thus demonstrating that the P3HT polaron population was enhanced to a much larger degree than the exciton population in the hybrid MoS_2–organic heterojunction employing the plasmonic metasurface. In addition to ultrafast hole transfer between MoS_2 and P3HT, which occurred both within the absorption band of P3HT (*i.e.*, 400 nm pump, Figure 2a) and for sub-band-gap wavelengths (*i.e.*, 800 nm pump, Supporting Information Figure S5), the enhanced $\Delta R/R$ signal for the hybrid P3HT:PCBM/MoS_2 active layer employing the plasmonic metasurface arose from increased absorption in both the MoS_2 and P3HT:PCBM layers, as demonstrated below.

For all pump and probe wavelengths, the P3HT polarons and excitons showed the same decay dynamics for both P3HT:PCBM and P3HT:PCBM/MoS_2, with and without the metasurface, within the first 10 ps (see Supporting Information Figure S8 and Table S1). However, the nanosecond-scale decay dynamics of the P3HT polarons were significantly modified for the hybrid MoS_2–organic active layer, with and without the metasurface (Figure 3). Over the 1 ns time scale, the magnitude of the $\Delta R/R$ signal showed the same trend as the 10 ps time scales (Figure 3a). However, the P3HT polaron lifetime was reduced for the P3HT:PCBM/MoS_2 hybrid active layer relative

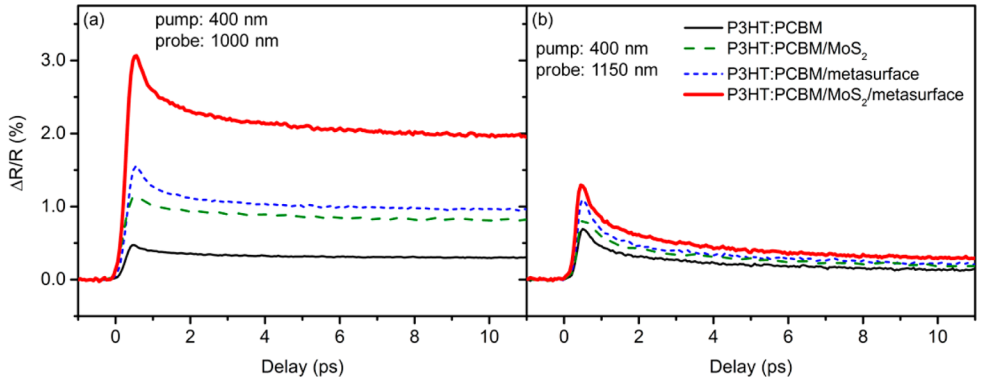

Figure 2. Picosecond-scale transient pump–probe reflection measurements from P3HT:PCBM and the hybrid P3HT:PCBM/MoS_2 active layers with and without the plasmonic metasurfaces using a pump wavelength of 400 nm and probe wavelengths of (a) 1000 nm (*i.e.*, probing the polaron and exciton dynamics in P3HT) and (b) 1150 nm (*i.e.*, probing the exciton dynamics in P3HT).

DOI: 10.1021/acsnano.6b03414
ACS Nano XXXX, XXX, XXX–XXX

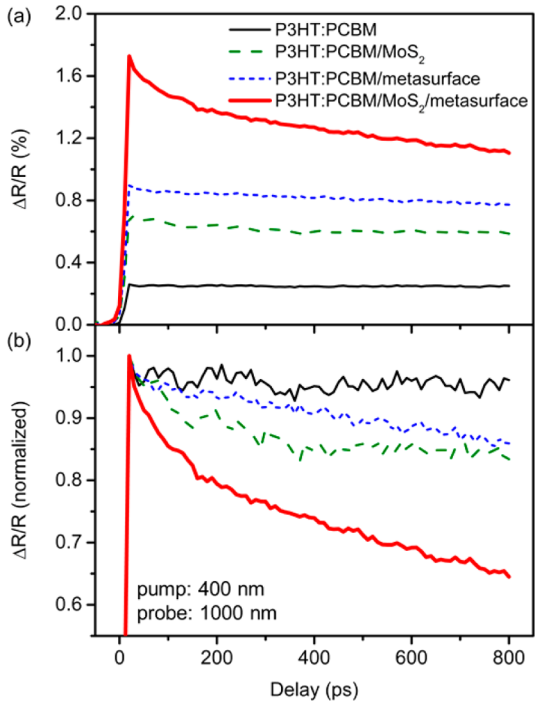

Figure 3. Nanosecond-scale transient pump−probe reflection measurements from P3HT:PCBM and the hybrid P3HT:PCBM/MoS_2 active layers with and without the plasmonic metasurfaces using a pump wavelength of 400 nm and a probe wavelength of 1000 nm: (a) magnitude of transient reflectometry; (b) normalized data.

to P3HT:PCBM alone (Figure 3b; Supporting Information Figure S9 and Table S2). The presence of the MoS_2 resulted in an extra decay component, with a decay constant of ∼160 ps, compared to P3HT:PCBM alone, which was fit to a constant value within this time regime. This extra decay component corresponded to the excess polarons transferred to the P3HT from the MoS_2. The presence of the plasmonic metasurface resulted in an additional decay component in the hybrid P3HT:PCBM/MoS_2 active layer (Figure 3b; Supporting Information Figure S9 and Table S2). For the hybrid active layer with the plasmonic metasurface, the fast decay component was ∼70 ps, and the slow component was ∼3 ns. These two components correspond to the excess polarons transferred to the P3HT from the MoS_2 (fast component) in addition to the excess polarons generated from the plasmonic metasurface (slow component). The lifetimes of these P3HT polarons were reduced relative to P3HT:PCBM/MoS_2 (160 ps) or P3HT:PCBM/metasurface (∼7 ns) alone due to the larger population of carriers within the P3HT:PCBM layer, since carrier concentration is inversely proportional to carrier lifetime.[75] However, even with the reduced polaron lifetime for the hybrid P3HT:PCBM/MoS_2 active layer with the metasurface, the overall polaron population was still more than 4 times higher than that of the P3HT:PCBM alone after 800 ps (Figure 3a). This suggests that a greater population of free charges will be available for collection at the respective electrodes for the hybrid P3HT:PCBM/MoS_2 active layer with the plasmonic metasurface. The larger P3HT polaron population within the hybrid P3HT:PCBM/MoS_2 active layer with the plasmonic metasurface is further confirmed by the enhanced photoluminescence (PL) from P3HT:PCBM (Supporting Information Figure S10).

Having demonstrated increased photogeneration in the hybrid P3HT:PCBM/MoS_2 active layer in the presence of the plasmonic metasurface, we now turn our attention to the impact of the plasmonic metasurfaces on the active layer absorption. We performed steady-state extinction measure-

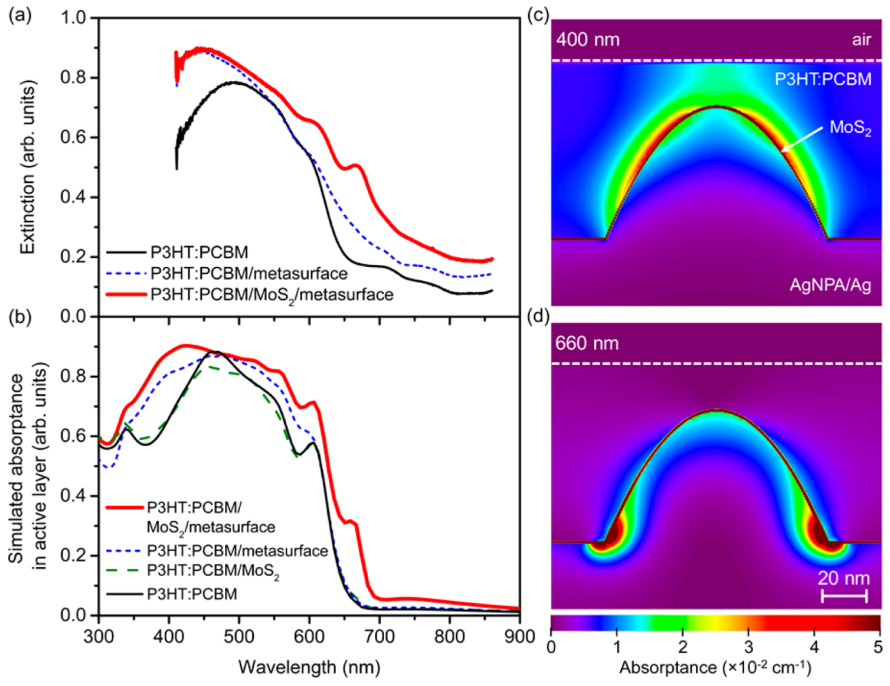

Figure 4. (a) Microscope-coupled extinction measurements from P3HT:PCBM and the hybrid P3HT:PCBM/MoS_2 active layers with and without the plasmonic metasurface. (b) Simulated active layer absorptance, defined as the P3HT:PCBM absorptance plus the MoS_2 absorptance. (c, d) Spatially varying cross-sectional simulated absorptance in the heterostructure at two different wavelengths: (c) 400 nm and (d) 660 nm. The plots in (c) and (d) are on the same scale, and the scale bar is shown in (d).

DOI: 10.1021/acsnano.6b03414
ACS Nano XXXX, XXX, XXX−XXX

ments using a microscope-coupled spectrometer on the hybrid P3HT:PCBM/MoS_2 active layer with and without the metasurface (Figure 4a). Comparing the hybrid P3HT:PCBM/MoS_2 with the metasurface to P3HT:PCBM alone, we observed increased extinction across the visible spectrum, particularly for longer wavelengths, suggesting an increase in the absorption bandwidth. For P3HT:PCBM on the metasurface alone, the extinction was improved for shorter wavelengths, but only slightly for longer wavelengths, suggesting that the MoS_2 plays the dominant role in the improved extinction at longer wavelengths. For the hybrid P3HT:PCBM/MoS_2 active layer with the metasurface, we obtained extinction enhancement factors of 1.5 at 410 nm and 2.9 at 670 nm (Supporting Information Figure S11a) relative to P3HT:PCBM alone and a spectrally integrated extinction enhancement factor of 1.4.

To understand these differences and to distinguish between useful absorption (*i.e.*, absorptance in the active layers) and scattering within the extinction measurements, we performed finite-difference time-domain (FDTD) simulations (Figure 4b–d). As in the extinction measurements, we observed a generally broadband active layer absorptance increase for the P3HT:PCBM/MoS_2 active layer with the metasurface. The active layer absorptance enhancement was largest at wavelengths between 350–450 nm and ≥550 nm for the hybrid P3HT:PCBM/MoS_2 active layers in the presence of the metasurface (Figure 4b and Supporting Information Figure S11b). The reason for the absorptance enhancements at these wavelengths was due to the formation of plasmon–exciton hybrid modes. When plasmonic metasurfaces are coated by absorbers (such as MoS_2 or P3HT:PCBM), the plasmonic modes are known to demonstrate splitting from coupling with the excitonic transitions of the absorber.[48−50,76−84] The presence of the 80-nm-thick P3HT:PCBM layer red-shifted and split the plasmonic modes to a much larger degree than the monolayer MoS_2 alone, as identified by scattered-light simulations (Figure S11d). In the presence of the P3HT:PCBM (with or without MoS_2), the short wavelength plasmon–exciton mode led to the absorptance enhancements observed between 350 and 450 nm. However, the long-wavelength plasmon–exciton hybrid mode was red-shifted outside of the absorption band of P3HT:PCBM, but spectrally overlapped with the strong absorption features in MoS_2 between 550 and 700 nm.[36,37] This led to a greater than 10-fold absorptance enhancement within the MoS_2 layer for wavelengths between 550 and 900 nm (Figure S11c). Without the P3HT:PCBM, the absorptance enhancement within the MoS_2 was much lower for wavelengths greater than 500 nm (~5; Figure S11c). Thus, the synergistic effect of the P3HT:PCBM, MoS_2, and metasurface combined gave rise to the maximum absorptance within the active layer. As a result, the active layer absorptance bandwidth (*i.e.*, full-width, half-maximum) of the hybrid P3HT:PCBM/MoS_2 active layer in the presence of the plasmonic metasurface was increased by 90 nm relative to that of P3HT:PCBM alone. We calculated a spectrally integrated enhancement factor weighted by the AM1.5 solar spectrum of 1.3 for the hybrid P3HT:PCBM/MoS_2 active layer with the metasurface (compared to <1.1 for P3HT:PCBM with the metasurface and <1.0 for P3HT:PCBM/MoS_2 without the metasurface).

Figure 4c,d shows cross sections of the simulated spatially varying absorptance distribution for the hybrid P3HT:PCBM/MoS_2 active layer with the metasurface within the different layers at two different wavelengths (*i.e.*, 400 and 660 nm). At both wavelengths, absorptance was stronger in the MoS_2 than in the P3HT:PCBM, due to the stronger absorption coefficient of MoS_2 and its closer proximity to the metasurface. At 400 nm (Figure 4c), absorptance was strongest at the tip of the AgNP. This suggests that even though experimentally the MoS_2 film did not conform perfectly to the surface of the AgNPA (Figure 1d), absorptance in the MoS_2 should still be increased quite strongly due to the intense electromagnetic fields near the tips of the AgNPs. At 660 nm (Figure 4d and Supporting Information Figure S11b,c), active layer absorptance predominantly occurred in the MoS_2, and most of the absorptance in the MoS_2 was confined to the base of the AgNPs due to the coupling between the AgNPs with the planar Ag film.[50] Because the MoS_2 film remained rigid in some regions, sitting on top of several 10's of particles (dark regions in Figure 1d), the experimentally observed extinction enhancement was not maximized (*cf.* Supporting Information Figure S11a,b). This demonstrates the need to have a fully conformal coating of the MoS_2 on the AgNPs in order to achieve the maximum broadening of the active layer absorptance: if the MoS_2 is not in close contact with the base of the AgNPs, the long wavelength absorptance will not be maximized. Li *et al.* have recently demonstrated a method of achieving completely conformal coverage of a nanocone array using capillary-pressure-induced nanoindentation.[85]

Utilizing the demonstrated enhanced absorption and charge photogeneration due to the hybrid P3HT:PCBM/MoS_2 heterojunction with the plasmonic metasurface, we outline the combined mechanisms that would lead to enhanced solar cell device efficiencies, which are depicted in Figure 5. Upon photoexcitation (Figure 5a), both the MoS_2 and P3HT absorb light, promoting electrons from their valence band (VB) and highest occupied molecular orbital (HOMO) to their conduction band (CB) and lowest unoccupied molecular orbital (LUMO), respectively. In the first excited state, the electrons and holes are electrostatically bound, forming excitons. At the same time, surface plasmons are excited within the metasurface by a portion of the incident light, increasing the generation of excitons in both MoS_2 and P3HT. Since the CB of MoS_2 lies between the Fermi level (E_F) of Ag and the LUMO of P3HT, MoS_2 is expected to serve as an efficient electron transport layer. Due to the relatively low work function of Ag,[86] its E_F is pinned close to the CB of MoS_2, resulting in a much smaller barrier for electron collection than for hole collection.[87] In addition, based on their staggered energy levels, P3HT and MoS_2 form a type-II p–n heterojunction,[28−31] allowing for the efficient transfer of electrons from P3HT to MoS_2 and holes from MoS_2 to P3HT, forming positive polarons (Figure 5b). This was evidenced by the increased $\Delta R/R$ signal at 1000 nm within the time resolution of our ultrafast measurements (<100 fs). We note that CVD-grown MoS_2 typically exhibits n-type conduction in standard field-effect transistors[87−94] and in van der Waals heterojunctions,[95−100] demonstrating its use as an electron transport layer. By contrast, chemically exfoliated MoS_2 exhibits p-type conduction,[39,101] thus demonstrating its use as a hole transport layer.

CONCLUSION

In conclusion, we have demonstrated ultrafast hole transfer between an inorganic 2D material, MoS_2, and an organic semiconductor blend, P3HT:PCBM. We have observed a 6-fold increase in the P3HT polaron transient pump–probe

DOI: 10.1021/acsnano.6b03414
ACS Nano XXXX, XXX, XXX–XXX

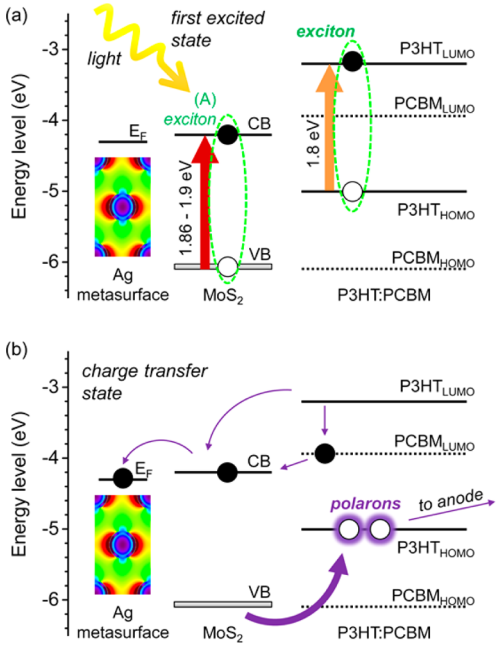

Figure 5. Energy level diagrams and photophysical processes for the different components of the hybrid P3HT:PCBM/MoS_2 active layer with the plasmonic metasurface for two different time scales: (a) instantaneously after photoexcitation, *i.e.*, carriers are promoted to the first excited state and the plasmonic modes of the metasurface are excited; (b) less than 100 fs after photoexcitation, when charge transfer processes occur. The black circles represent electrons, white circles represent holes; the orange arrow indicates the lowest energy absorption transition in P3HT; the red arrow indicates the lowest energy absorption transition in MoS_2; the purple arrows indicate the direction of charge transfer. [E_F = Fermi level;[86] CB = conduction band; VB = valence band;[36,102,103] LUMO = lowest unoccupied molecular orbital; HOMO = highest occupied molecular orbital[104,105]]. Note that due to the conformal nature of MoS_2 on the metasurface, the PL emission from MoS_2 shifted by 27 meV relative to planar MoS_2 (Supporting Information Figure S12).[85] This relatively small shift (represented by the width of the gray line for the VB of MoS_2) does not significantly influence the charge transfer between MoS_2 and P3HT.

signal in the hybrid P3HT:PCBM/MoS_2 heterojunction in the presence of a Ag nanoparticle array plasmonic metasurface, which we have shown was a result of the combined effects of absorption enhancement in both the P3HT:PCBM and MoS_2 layers combined with hole transfer from MoS_2 to P3HT. The hole transfer from MoS_2 was observed at both 400 and 800 nm pump wavelengths, demonstrating that hole transfer occurs both within the absorption band of P3HT and for sub-band-gap wavelengths. We observed an increase in the active layer absorption bandwidth of 90 nm through reflection measurements and optical simulations for the hybrid P3HT:PCBM/MoS_2 active layer in the presence of plasmonic metasurface. Future work includes fabricating full photovoltaic devices employing hybrid 2D−organic heterojunctions, with and without plasmonic metasurfaces to make use of the broadened and enhanced solar spectrum. The enhancements we observed in these hybrid P3HT:PCBM/MoS_2 active layers in the presence of the plasmonic metasurface could also be applied to other thin-film photovoltaic active layers, such as amorphous Si, CdTe, or hybrid organic−inorganic perovskites.

METHODS

Template-Based Fabrication of Plasmonic Metasurfaces. The procedure to prepare a disordered Ag nanoparticle array on Ag thin-film (*i.e.*, AgNPA/Ag) plasmonic metasurfaces has been described previously.[50] Briefly, 150 nm Ag was deposited onto cleaned glass substrates with a 5 nm Cr adhesion layer using thermal evaporation (chamber pressure less than 8×10^{-6} mbar for each evaporation, and the deposition rate was less than or equal to 0.1 nm/s). Through-hole anodic aluminum oxide (AAO) nanotemplates (Synkera Inc.) with an average pore diameter of 55 nm and AAO thickness of 500 nm were employed as shadow masks for the growth of the nanoparticles (NPs). The pores of the AAO nanotemplate were widened to ∼100 nm by soaking the nanotemplates in aqueous H_3PO_4 (5%, w/w) at 30 °C for 30 min. The nanotemplates were transferred to the Ag films, through which 60 nm Ag was evaporated to achieve AgNPs of ∼60 nm height and ∼100 nm diameter.

MoS_2 Growth and Transfer. Single-layer MoS_2 nanosheets were grown by CVD using MoO_3 (Sigma-Aldrich, 50 mg) and sulfur (Sigma-Aldrich, 250 mg) powders as solid precursors. SiO_2/Si wafers (2 cm × 1 cm), facing up, were placed above the MoO_3 powder in the center of a 1-in. quartz tube in the hot region of the furnace. Sulfur was located upstream at the entrance of the furnace (∼20 cm from the MoO_3 boat). Prior to growth, air was evacuated by flowing Ar (ultrahigh purity, Air Gas) for 15 min at 200 sccm, after which the tube was heated at 200 °C for 15 min to remove moisture from the precursors. The temperature was then increased to 750 °C under a 90 sccm Ar flow. After 45 min, the furnace was naturally cooled to room temperature and samples were removed from the tube.

The wafers were further observed by bright-field optical microscopy. Individual MoS_2 crystals are typically between 5 and 30 μm in size (Supporting Information Figure S1a−c) and grow in the center of the wafer. When looking closer to the edge of the wafer located upstream, the size of the crystals increases. The crystals eventually get connected (Supporting Information Figure S1d−f), and a continuous single-layer MoS_2 film starts to form. Large-area polycrystalline domains without pinholes can be obtained with dimensions over 1 mm^2 (Supporting Information Figure S1g−i).

MoS_2 on SiO_2/Si wafers was transferred on Ag and metasurface substrates using poly(methyl methacrylate) (PMMA). A6 PMMA was spin-coated on the SiO_2/Si wafer covered with the MoS_2 nanosheets (4000 rpm for 45 s) and baked at 120 °C for 5 min to ensure good adhesion between MoS_2 and PMMA. The wafer was then etched using a 1 M NaOH solution at 50 °C. After delamination, the PMMA layer was transferred on various substrates and dried in air. Once dried in air, the substrates were further dried under vacuum for 5 h. Finally the PMMA layer was then dissolved using acetone (4 × 50 mL).

Polymer:Fullerene Solution and Thin-Film Preparation. P3HT (Rieke Polymers, product number RMI-001EE; M_w 69 000 g mol^{-1}; polydispersity index 2.3; regioregularity 96%) and PCBM (ONE Material, product number OS0266) in a 1:1 ratio were dissolved in chlorobenzene (40 g L^{-1} total blend concentration) by heating to 60 °C while stirring at 1200 rpm for >5 h. The solution was then filtered through a 0.2 μm pore regenerated cellulose filter prior to spin-coating. The solution was spin-coated onto the various substrates (planar Ag, Ag metasurface, MoS_2/Ag, and MoS_2/metasurface) at 5000 rpm to achieve P3HT:PCBM coatings of ∼80 nm, as confirmed through atomic force microscopy measurements.

Ultrafast Two-Color Pump−Probe Reflection Measurements. Ultrafast two-color transient pump−probe reflection measurements were obtained using a 1 kHz, 800 nm, 70 fs Ti:sapphire amplified laser (Spectra-Physics Spitfire Ace). We used pump wavelengths of either 400 nm, by frequency doubling a portion of the fundamental 800 nm laser output, or 800 nm itself. The pump was chopped at 500 Hz, and a fluence of ∼25 μJ cm^{-2} was used to minimize damage to the P3HT:PCBM film during the measurements (see Supporting Information Figure S13 for stability tests). The remainder of the laser power was directed to an optical parametric amplifier (Spectra-Physics TOPAS prime) to generate probe wavelengths of either 1000 or 1150 nm. The reflected probe beam

DOI: 10.1021/acsnano.6b03414
ACS Nano XXXX, XXX, XXX−XXX

(diameter ~75 μm) was directed to a lock-in amplifier to collect the signal, and a fluence of ~5 μJ cm^{-2} was used. A delay stage step size of 50 fs was used for the 10 ps dynamics, and a step size of 10 ps was used for the 800 ps dynamics. For all measurements, at least 20 scans were averaged to improve the signal-to-noise ratio. Note that for the 800 nm pump/1000 nm probe measurements, the pump fluence was increased to ~240 μJ cm^{-2}.

Steady-State Optical Spectroscopy. Extinction measurements were obtained using a microscope-coupled spectrometer (Tokyo Instruments Nanofinder 30) using halogen lamp illumination and a 100× microscope objective (NA = 0.95). Bright-field (BF) reflected-light spectra of the selected region (BF_{sample}) were acquired using a pinhole diameter of 250 μm, in addition to an exposure time of 50 ms with 10 accumulations. After binning, the total area from which the spectra were collected was approximately 5 μm^2. Spectra were collected from a minimum of three regions for the most uniform samples (*i.e.*, for P3HT:PCBM) and a maximum of seven regions for the most nonuniform samples (*i.e.*, for P3HT:PCBM/MoS_2/metasurface; see Supporting Information Figure S14 for individual spectra). Background spectra were collected by blocking the light path to the spectrometer (BF_{bkgd}). Spectra were normalized to the lamp spectral intensity using the BF reflection spectrum from a planar Ag film (BF_{Ag}). Extinction was calculated using eq 1:

$$\text{Extinction} = 1 - \frac{BF_{sample} - BF_{bkgd}}{BF_{Ag} - BF_{bkgd}} \quad (1)$$

Dark-field (DF) scattered-light images were acquired using an Olympus BX51 under xenon lamp illumination in reflection mode with a 10× DF microscope objective (NA = 0.30).

Finite-Difference Time-Domain Simulations. FDTD simulations were conducted as described previously using commercially available software (Lumerical FDTD Solutions).[50,106] Briefly, a hexagonally packed array of paraboloids was used to simulate the AgNPs having heights of 60 nm, base diameters of 100 nm, and a period of 150 nm. The structures were defined in the software to match the fabricated plasmonic metasurfaces as closely as possible (80 nm P3HT:PCBM coating/AgNPA/150 nm Ag/5 nm Cr/glass). For the hybrid MoS_2/organic heterostructures, monolayer MoS_2 (thickness of 0.67 nm) was used to conformally coat the AgNPs. This idealized, periodic structure does not perfectly match the experimentally prepared MoS_2–metasurface heterostructures, but the main differences are described in the text. The optical constants used for each layer were obtained from the literature (Supporting Information Figure S15). The excitation source used was a total-field scattered-field (TFSF) plane wave incident at 5° from the surface normal using transverse magnetic polarization. The wavelength range of the source was 300–900 nm with 5 nm increments and a source pulse length of 1.995 fs. Bloch boundary conditions were used in the planes normal to the substrate, and perfectly matched layers were used in the plane parallel to the substrate. A mesh of 2 nm spacing was used throughout the heterostructure, except where override regions were included. A mesh override region of 0.6 nm in the lateral directions (x, y) and 0.4 nm in the surface normal direction (z) was used for the region surrounding the AgNPs, and an override region of 0.3 nm in the z-direction was used for the region surrounding the planar MoS_2 at the base of the AgNPs. The scattered-light spectra were acquired by taking the transmission through a frequency-dependent power monitor located outside of the TFSF source. For the absorption simulations, a fully three-dimensional frequency-domain power monitor was placed surrounding the thin-film stack to obtain the electric field intensity at every position and wavelength. A three-dimensional refractive index monitor was overlaid on the frequency-domain power monitor. The fields were sampled every other mesh point due to the finite computational memory associated with three-dimensional field and index monitors.

As described in prior published work,[50] absorptance in each layer was calculated using the following equation:

$$A(x, y, z, \lambda) = n(x, y, z, \lambda)\, \alpha(x, y, z, \lambda) \left| \frac{E(x, y, z, \lambda)}{E_0} \right|^2 \quad (2)$$

where n is the real part of the complex index of refraction, α is the attenuation coefficient ($4\pi k/\lambda$), and $|E/E_0|^2$ is the normalized electric field intensity squared. The absorptance was integrated spatially and normalized to the area illuminated (S_{illum}) to obtain the spectral fraction of light absorbed in each layer:

$$A(\lambda) = \frac{\int_x \int_y \int_z A(x, y, z, \lambda)\, \partial x\, \partial y\, \partial z}{S_{illum}} \quad (3)$$

The absorptance in the P3HT:PCBM and MoS_2 layers (Supporting Information Figure S11b,c) were separated from each other and from the absorptance in the AgNPA by using the refractive index monitor as a reference. Finally, the spatially integrated absorptance in each layer was weighted by the AM1.5 solar spectrum ($P_{AM1.5}$) and integrated over all wavelengths:

$$A = \frac{\int_\lambda P_{AM1.5}(\lambda)\, A(\lambda)\, \partial\lambda}{\int_\lambda P_{AM1.5}(\lambda)\, \partial\lambda} \quad (4)$$

FDTD simulations were also conducted for planar Ag electrodes. These simulations were identical to the absorption enhancement simulations containing the AgNPA, except that the AgNPAs were removed. Absorptance enhancement factors were calculated by dividing absorptance in the active layer coating the AgNPA/Ag substrates by the absorptance in the active layer coating the planar Ag substrates.

ASSOCIATED CONTENT

Supporting Information

The Supporting Information is available free of charge on the ACS Publications website at DOI: 10.1021/acsnano.6b03414.

Additional details about the sample preparation and ultrafast measurements; pump–probe reflectometry for 800 nm pump and 1000 nm probe; fitting analysis for the polaron and exciton dynamics; photoluminescence spectra from P3HT:PCBM, MoS_2, and the hybrid P3HT:PCBM/MoS_2 with and without the plasmonic metasurface; additional FDTD simulation details and optical constants obtained from the literature (PDF)

AUTHOR INFORMATION

Corresponding Author

*E-mail: c.petoukhoff@rutgers.edu.

ORCID

Christopher E. Petoukhoff: 0000-0001-6786-8830

Present Address

⊥Institut Européen des Membranes, University of Montpellier, Place Eugène Bataillon, 34095 Montpellier, France.

Notes

The authors declare no competing financial interest.

ACKNOWLEDGMENTS

This material is based upon work supported by the National Science Foundation (NSF) under Grant No. 1515423, "East Asia and Pacific Summer Institutes", and NSF Grant No. DMR-1309459. We thank J. Madéo, T. Harada, K. Deasy, D. Renaud, and A. Gilman for useful discussions.

DOI: 10.1021/acsnano.6b03414
ACS Nano XXXX, XXX, XXX–XXX

REFERENCES

(1) Shah, A.; Torres, P.; Tscharner, R.; Wyrsch, N.; Keppner, H. Photovoltaic Technology: The Case for Thin-Film Solar Cells. *Science* **1999**, *285*, 692−698.

(2) Huang, J.; Li, G.; Yang, Y. A Semi-Transparent Plastic Solar Cell Fabricated by a Lamination Process. *Adv. Mater.* **2008**, *20*, 415−419.

(3) Lee, K.-T.; Lee, J. Y.; Seo, S.; Guo, L. J. Colored Ultrathin Hybrid Photovoltaics with High Quantum Efficiency. *Light: Sci. Appl.* **2014**, *3*, e215.

(4) Krebs, F. C.; Hösel, M. The Solar Textile Challenge: How It Will Not Work and Where It Might. *ChemSusChem* **2015**, *8*, 966−969.

(5) Noh, J. H.; Im, S. H.; Heo, J. H.; Mandal, T. N.; Seok, S. I. Chemical Management for Colorful, Efficient, and Stable Inorganic-Organic Hybrid Nanostructured Solar Cells. *Nano Lett.* **2013**, *13*, 1764−1769.

(6) Lee, M. M.; Teuscher, J.; Miyasaka, T.; Murakami, T. N.; Snaith, H. J. Efficient Hybrid Solar Cells Based on Meso-Superstructured Organometal Halide Perovskites. *Science* **2012**, *338*, 643−647.

(7) Brenner, T. M.; Egger, D. A.; Kronik, L.; Hodes, G.; Cahen, D. Hybrid Organic-Inorganic Perovskites: Low-Cost Semiconductors with Intriguing Charge-Transport Properties. *Nat. Rev. Mater.* **2016**, *1*, 15007.

(8) Moon, S. J.; Baranoff, E.; Zakeeruddin, S. M.; Yeh, C. Y.; Diau, E. W. G.; Grätzel, M.; Sivula, K. Enhanced Light Harvesting in Mesoporous TiO_2/P3HT Hybrid Solar Cells Using a Porphyrin Dye. *Chem. Commun.* **2011**, *47*, 8244−8246.

(9) Kang, M. G.; Park, N.-G.; Park, Y. J.; Ryu, K. S.; Chang, S. H. Manufacturing Method for Transparent Electric Windows Using Dye-Sensitized TiO_2 Solar Cells. *Sol. Energy Mater. Sol. Cells* **2003**, *75*, 475−479.

(10) Kojima, A.; Teshima, K.; Shirai, Y.; Miyasaka, T. Organometal Halide Perovskites as Visible-Light Sensitizers for Photovoltaic Cells. *J. Am. Chem. Soc.* **2009**, *131*, 6050−6051.

(11) Yang, W. S.; Noh, J. H.; Jeon, N. J.; Kim, Y. C.; Ryu, S.; Seo, J.; Seok, S. I. High-Performance Photovoltaic Perovskite Layers Fabricated through Intramolecular Exchange. *Science* **2015**, *348*, 1234−1237.

(12) Huynh, W. U.; Dittmer, J. J.; Alivisatos, A. P.Hybrid Nanorod-Polymer Solar Cells. *Science***2002**, *295*.242510.1126/science.1069156

(13) Plass, R.; Pelet, S.; Krueger, J.; Grätzel, M.; Bach, U. Quantum Dot Sensitization of Organic-Inorganic Hybrid Solar Cells. *J. Phys. Chem. B* **2002**, *106*, 7578−7580.

(14) Sun, B.; Marx, E.; Greenham, N. C. Photovoltaic Devices Using Blends of Branched CdSe Nanoparticles and Conjugated Polymers. *Nano Lett.* **2003**, *3*, 961−963.

(15) Beek, W. J. E.; Wienk, M. M.; Janssen, R. A. J. Efficient Hybrid Solar Cells from Zinc Oxide Nanoparticles and a Conjugated Polymer. *Adv. Mater.* **2004**, *16*, 1009−1013.

(16) Beek, W. J. E.; Wienk, M. M.; Janssen, R. A. J. Hybrid Solar Cells from Regioregular Polythiophene and ZnO Nanoparticles. *Adv. Funct. Mater.* **2006**, *16*, 1112−1116.

(17) Boschloo, G.; Hagfeldt, A. Characteristics of the Iodide/Triiodide Redox Mediator in Dye-Sensitized Solar Cells. *Acc. Chem. Res.* **2009**, *42*, 1819−1826.

(18) Chen, P.; Yum, J. H.; De Angelis, F.; Mosconi, E.; Fantacci, S.; Moon, S.-J.; Baker, R. H.; Ko, J.; Nazeeruddin, M. K.; Grätzel, M. High Open-Circuit Voltage Solid-State Dye-Sensitized Solar Cells with Organic Dye. *Nano Lett.* **2009**, *9*, 2487−2492.

(19) O'Reagen, B.; Grätzel, M. A Low-Cost, High-Efficiency Solar Cell Based on Dye-Sensitized Colloidal TiO_2 Films. *Nature* **1991**, *353*, 737−740.

(20) Hardin, B. E.; Snaith, H. J.; McGehee, M. D. The Renaissance of Dye-Sensitized Solar Cells. *Nat. Photonics* **2012**, *6*, 162−169.

(21) Heeger, A. J. Nobel Lecture: Semiconducting and Metallic Polymers: The Fourth Generation of Polymeric Materials. *Rev. Mod. Phys.* **2001**, *73*, 681−700.

(22) Søndergaard, R.; Helgesen, M.; Jørgensen, M.; Krebs, F. C. Fabrication of Polymer Solar Cells Using Aqueous Processing for All Layers Including the Metal Back Electrode. *Adv. Energy Mater.* **2011**, *1*, 68−71.

(23) Campoy-Quiles, M.; Heliotis, G.; Xia, R.; Ariu, M.; Pintani, M.; Etchegoin, P.; Bradley, D. D. C. Ellipsometric Characterization of the Optical Constants of Polyfluorene Gain Media. *Adv. Funct. Mater.* **2005**, *15*, 925−933.

(24) Hide, F.; Díaz-García, M.; Schwartz, B. J.; Andersson, M. R.; Pei, Q.; Heeger, A. J. Semiconducting Polymers: A New Class of Solid-State Laser Materials. *Science* **1996**, *273*, 1833−1836.

(25) McCullough, R. D. The Chemistry of Conducting Polythiophenes. *Adv. Mater.* **1999**, *10*, 93−116.

(26) Morin, J.-F.; Leclerc, M.; Adès, D.; Siove, A. Polycarbazoles: 25 Years of Progress. *Macromol. Rapid Commun.* **2005**, *26*, 761−778.

(27) Heeger, A. J. 25th Anniversary Article: Bulk Heterojunction Solar Cells: Understanding the Mechanism of Operation. *Adv. Mater.* **2014**, *26*, 10−27.

(28) He, D.; Pan, Y.; Nan, H.; Gu, S.; Yang, Z.; Wu, B.; Luo, X.; Xu, B.; Zhang, Y.; Li, Y.; et al. A van der Waals pn Heterojunction with Organic/Inorganic Semiconductors. *Appl. Phys. Lett.* **2015**, *107*, 183103.

(29) Jariwala, D.; Howell, S. L.; Chen, K. S.; Kang, J.; Sangwan, V. K.; Filippone, S. A.; Turrisi, R.; Marks, T. J.; Lauhon, L. J.; Hersam, M. C. Hybrid, Gate-Tunable, van der Waals p-n Heterojunctions from Pentacene and MoS_2. *Nano Lett.* **2016**, *16*, 497−503.

(30) Liu, F.; Chow, W. L.; He, X.; Hu, P.; Zheng, S.; Wang, X.; Zhou, J.; Fu, Q.; Fu, W.; Yu, P.; et al. Van der Waals p-n Junction Based on an Organic-Inorganic Heterostructure. *Adv. Funct. Mater.* **2015**, *25*, 5865−5871.

(31) Vélez, S.; Ciudad, D.; Island, J.; Buscema, M.; Txoperena, O.; Parui, S.; Steele, G. A.; Casanova, F.; van der Zant, H. S.; Castellanos-Gomez, A.; et al. Gate-Tunable Diode and Photovoltaic Effect in an Organic-2D Layered Material p-n Junction. *Nanoscale* **2015**, *7*, 15442−15449.

(32) Chhowalla, M.; Shin, H. S.; Eda, G.; Li, L. J.; Loh, K. P.; Zhang, H. The Chemistry of Two-Dimensional Layered Transition Metal Dichalcogenide Nanosheets. *Nat. Chem.* **2013**, *5*, 263−275.

(33) Das, S.; Robinson, J. A.; Dubey, M.; Terrones, H.; Terrones, M. Beyond Graphene: Progress in Novel Two-Dimensional Materials and van der Waals Solids. *Annu. Rev. Mater. Res.* **2015**, *45*, 1−27.

(34) Geim, A. K.; Grigorieva, I. V. Van der Waals Heterostructures. *Nature* **2013**, *499*, 419−425.

(35) Korn, T.; Heydrich, S.; Hirmer, M.; Schmutzler, J.; Schüller, C. Low-Temperature Photocarrier Dynamics in Monolayer MoS_2. *Appl. Phys. Lett.* **2011**, *99*, 102109:1−3.

(36) Mak, K. F.; Lee, C.; Hone, J.; Shan, J.; Heinz, T. F. Atomically Thin MoS_2: A New Direct-Gap Semiconductor. *Phys. Rev. Lett.* **2010**, *105*, 136805:1−4.

(37) Splendiani, A.; Sun, L.; Zhang, Y.; Li, T.; Kim, J.; Chim, C. Y.; Galli, G.; Wang, F. Emerging Photoluminescence in Monolayer MoS_2. *Nano Lett.* **2010**, *10*, 1271−1275.

(38) Bernardi, M.; Palummo, M.; Grossman, J. C. Extraordinary Sunlight Absorption and One Nanometer Thick Photovoltaics Using Two-Dimensional Monolayer Materials. *Nano Lett.* **2013**, *13*, 3664−3670.

(39) Gu, X.; Cui, W.; Li, H.; Wu, Z.; Zeng, Z.; Lee, S.-T.; Zhang, H.; Sun, B. A Solution-Processed Hole Extraction Layer Made from Ultrathin MoS_2 Nanosheets for Efficient Organic Solar Cells. *Adv. Energy Mater.* **2013**, *3*, 1262−1268.

(40) Tsai, M.-L.; Su, S.-H.; Chang, J.-K.; Tsai, D.-S.; Chen, C.-H.; Wu, C.-I.; Li, L.-J.; Chen, L.-J.; He, J.-H. Monolayer MoS_2 Heterojunction Solar Cells. *ACS Nano* **2014**, *8*, 8317−8322.

(41) Eda, G.; Yamaguchi, H.; Voiry, D.; Fujita, T.; Chen, M.; Chhowalla, M. Photoluminescence from Chemically Exfoliated MoS_2. *Nano Lett.* **2011**, *11*, 5111−5116.

(42) Shanmugam, M.; Bansal, T.; Durcan, C. A.; Yu, B. Molybdenum Disulphide/Titanium Dioxide Nanocomposite-Poly 3-Hexylthiophene Bulk Heterojunction Solar Cell. *Appl. Phys. Lett.* **2012**, *100*, 153901:1−4.

DOI: 10.1021/acsnano.6b03414
ACS Nano XXXX, XXX, XXX−XXX

(43) Yim, C.; O'Brien, M.; McEvoy, N.; Winters, S.; Mirza, I.; Lunney, J. G.; Duesberg, G. S. Investigation of the Optical Properties of MoS_2 Thin Films Using Spectroscopic Ellipsometry. *Appl. Phys. Lett.* **2014**, *104*, 103114:1−5.
(44) Park, J. W.; So, H. S.; Kim, S.; Choi, S.-H.; Lee, H.; Lee, J.; Lee, C.; Kim, Y. Optical Properties of Large-Area Ultrathin MoS_2 Films: Evolution from a Single Layer to Multilayers. *J. Appl. Phys.* **2014**, *116*, 183509:1−6.
(45) Clarke, T. M.; Peet, J.; Nattestad, A.; Drolet, N.; Dennler, G.; Lungenschmied, C.; Leclerc, M.; Mozer, A. J. Charge Carrier Mobility, Bimolecular Recombination and Trapping in Polycarbazole Copolymer:Fullerene (PCDTBT:PCBM) Bulk Heterojunction Solar Cells. *Org. Electron.* **2012**, *13*, 2639−2646.
(46) Gan, Q.; Bartoli, F. J.; Kafafi, Z. H. Plasmonic-Enhanced Organic Photovoltaics: Breaking the 10% Efficiency Barrier. *Adv. Mater.* **2013**, *25*, 2385−2396.
(47) Mihailetchi, V. D.; Xie, H.; de Boer, B.; Koster, L. J. A.; Blom, P. W. M. Charge Transport and Photocurrent Generation in Poly(3-Hexylthiophene): Methanofullerene Bulk-Heterojunction Solar Cells. *Adv. Funct. Mater.* **2006**, *16*, 699−708.
(48) Adato, R.; Artar, A.; Erramilli, S.; Altug, H. Engineered Absorption Enhancement and Induced Transparency in Coupled Molecular and Plasmonic Resonator Systems. *Nano Lett.* **2013**, *13*, 2584−2591.
(49) Antosiewicz, T. J.; Apell, S. P.; Shegai, T. Plasmon−Exciton Interactions in a Core−Shell Geometry: From Enhanced Absorption to Strong Coupling. *ACS Photonics* **2014**, *1*, 454−463.
(50) Petoukhoff, C. E.; O'Carroll, D. M. Absorption-Induced Scattering and Surface Plasmon Out-Coupling from Absorber-Coated Plasmonic Metasurfaces. *Nat. Commun.* **2015**, *6*, 7899:1−13.
(51) Bai, W.; Gan, Q.; Song, G.; Chen, L.; Kafafi, Z. H.; Bartoli, F. J. Broadband Short-Range Surface Plasmon Structures for Absorption Enhancement in Organic Photovoltaics. *Opt. Express* **2010**, *18*, A620−A630.
(52) Choy, W. C. H. The Emerging Multiple Metal Nanostructures for Enhancing the Light Trapping of Thin Film Organic Photovoltaic Cells. *Chem. Commun.* **2014**, *50*, 11984−11993.
(53) Yu, B.; Goodman, S.; Abdelaziz, A.; O'Carroll, D. M. Light-Management in Ultra-Thin Polythiophene Films Using Plasmonic Monopole Nanoantennas. *Appl. Phys. Lett.* **2012**, *101*, 151106:1−4.
(54) Yu, B.; Woo, J.; Kong, M.; O'Carroll, D. M. Mode-Specific Study of Nanoparticle-Mediated Optical Interactions in an Absorber/Metal Thin Film System. *Nanoscale* **2015**, *7*, 13196−13206.
(55) Eda, G.; Maier, S. A. Two-Dimensional Crystals: Managing Light for Optoelectronics. *ACS Nano* **2013**, *7*, 5660−5665.
(56) Jariwala, D.; Davoyan, A. R.; Tagliabue, G.; Sherrott, M. C.; Wong, J.; Atwater, H. A. Near-Unity Absorption in van der Waals Semiconductors for Ultrathin Optoelectronics. *Nano Lett.* **2016**, *16*, 5482.
(57) Li, Z.; Xiao, Y.; Gong, Y.; Wang, Z.; Kang, Y.; Zu, S.; Ajayan, P. M.; Nordlander, P.; Fang, Z. Active Light Control of the MoS_2 Monolayer Exciton Binding Energy. *ACS Nano* **2015**, *9*, 10158−10164.
(58) Lin, J.; Li, H.; Zhang, H.; Chen, W. Plasmonic Enhancement of Photocurrent in MoS_2 Field-Effect-Transistor. *Appl. Phys. Lett.* **2013**, *102*, 203109.
(59) Lee, B.; Park, J.; Han, G. H.; Ee, H. S.; Naylor, C. H.; Liu, W.; Johnson, A. T. C.; Agarwal, R. Fano Resonance and Spectrally Modified Photoluminescence Enhancement in Monolayer MoS_2 Integrated with Plasmonic Nanoantenna Array. *Nano Lett.* **2015**, *15*, 3646−3653.
(60) Butun, S.; Tongay, S.; Aydin, K. Enhanced Light Emission from Large-Area Monolayer MoS_2 Using Plasmonic Nanodisc Arrays. *Nano Lett.* **2015**, *15*, 2700−2704.
(61) Najmaei, S.; Mlayah, A.; Arbouet, A.; Girard, C.; Léotin, J.; Lou, J. Plasmonic Pumping of Excitonic Photoluminescence in Hybrid MoS_2-Au Nanostructures. *ACS Nano* **2014**, *8*, 12682−12689.
(62) Sobhani, A.; Lauchner, A.; Najmaei, S.; Ayala-Orozco, C.; Wen, F.; Lou, J.; Halas, N. J. Enhancing the Photocurrent and Photoluminescence of Single Crystal Monolayer MoS_2 with Resonant Plasmonic Nanoshells. *Appl. Phys. Lett.* **2014**, *104*, 031112.
(63) Yu, Y.; Ji, Z.; Zu, S.; Du, B.; Kang, Y.; Li, Z.; Zhou, Z.; Shi, K.; Fang, Z. Ultrafast Plasmonic Hot Electron Transfer in Au Nanoantenna/MoS_2 Heterostructures. *Adv. Funct. Mater.* **2016**, *26*, 6394.
(64) Wang, Z.; Dong, Z.; Gu, Y.; Chang, Y. H.; Zhang, L.; Li, L. J.; Zhao, W.; Eda, G.; Zhang, W.; Grinblat, G.; et al. Giant Photoluminescence Enhancement in Tungsten-Diselenide-Gold Plasmonic Hybrid Structures. *Nat. Commun.* **2016**, *7*, 11283.
(65) Atwater, H. A.; Polman, A. Plasmonics for Improved Photovoltaic Devices. *Nat. Mater.* **2010**, *9*, 205−213.
(66) Ferry, V. E.; Munday, J. N.; Atwater, H. A. Design Considerations for Plasmonic Photovoltaics. *Adv. Mater.* **2010**, *22*, 4794−4808.
(67) Munday, J. N.; Atwater, H. A. Large Integrated Absorption Enhancement in Plasmonic Solar Cells by Combining Metallic Gratings and Antireflection Coatings. *Nano Lett.* **2011**, *11*, 2195−2201.
(68) Nemes, C. T.; Vijapurapu, D. K.; Petoukhoff, C. E.; Cheung, G. Z.; O'Carroll, D. M. Absorption and Scattering Effects by Silver Nanoparticles near the Interface of Organic/Inorganic Semiconductor Tandem Films. *J. Nanopart. Res.* **2013**, *15*, 1801:1−13.
(69) O'Carroll, D. M.; Collopy, A. X.; Ferry, V. E.; Atwater, H. A. In *Surface Plasmon Assisted Absorption in Conjugated Polymer Thin Films and Devices*, 25th European Photovoltaic Solar Energy Conference, Valencia, Spain, 2010; pp 834−837.
(70) Lee, C.; Yan, H.; Brus, L. E.; Heinz, T. F.; Hone, J.; Ryu, S. Anomalous Lattice Vibrations of Single- and Few-Layer MoS_2. *ACS Nano* **2010**, *4*, 2695−2700.
(71) Guo, J.; Ohkita, H.; Benten, H.; Ito, S. Charge Generation and Recombination Dynamics in Poly(3-Hexylthiophene)/Fullerene Blend Films with Different Regioregularities and Morphologies. *J. Am. Chem. Soc.* **2010**, *132*, 6154−6164.
(72) Hwang, I.-W.; Moses, D.; Heeger, A. J. Photoinduced Carrier Generation in P3HT/PCBM Bulk Heterojunction Materials. *J. Phys. Chem. C* **2008**, *112*, 4350−4354.
(73) Wu, B.; Wu, X.; Guan, C.; Tai, K. F.; Yeow, E. K. L.; Fan, H. J.; Mathews, N.; Sum, T. C. Uncovering Loss Mechanisms in Silver Nanoparticle-Blended Plasmonic Organic Solar Cells. *Nat. Commun.* **2013**, *4*, 2004:1−7.
(74) Piris, J.; Dykstra, T. E.; Bakulin, A. A.; van Loosdrecht, P. H. M.; Knulst, W.; Trinh, M. T.; Schins, J. M.; Siebbeles, L. D. A. Photogeneration and Ultrafast Dynamics of Excitons and Charges in P3HT/PCBM Blends. *J. Phys. Chem. C* **2009**, *113*, 14500−14506.
(75) Sze, S. M.; Ng, K. K.*Physics of Semiconductor Devices*, 3rd ed.; John Wiley & Sons, Inc.: Hoboken, NJ, 2007.
(76) Bellessa, J.; Bonnand, C.; Plenet, J. C.; Mugnier, J. Strong Coupling between Surface Plasmons and Excitons in an Organic Semiconductor. *Phys. Rev. Lett.* **2004**, *93*, in press DOI: 10.1103/PhysRevLett.93.036404.
(77) Dintinger, J.; Klein, S.; Bustos, F.; Barnes, W. L.; Ebbesen, T. W. Strong Coupling between Surface Plasmon-Polaritons and Organic Molecules in Subwavelength Hole Arrays. *Phys. Rev. B: Condens. Matter Mater. Phys.* **2005**, *71*, in press DOI: 10.1103/PhysRevB.71.035424.
(78) Fofang, N. T.; Park, T.-H.; Neumann, O.; Mirin, N. A.; Nordlander, P.; Halas, N. J. Plexcitonic Nanoparticles: Plasmon-Exciton Coupling in Nanoshell-J-Aggregate Complexes. *Nano Lett.* **2008**, *8*, 3481−3487.
(79) Hranisavljevic, J.; Dimitrijevic, N. M.; Wurtz, G. A.; Wiederrecht, G. P. Photoinduced Charge Separation Reactions of J-Aggregates Coated on Silver Nanoparticles. *J. Am. Chem. Soc.* **2002**, *124*, 4536−4537.
(80) Pockrand, I.; Brillante, A.; Möbius, D. Exciton−Surface Plasmon Coupling: An Experimental Investigation. *J. Chem. Phys.* **1982**, *77*, 6289−6295.
(81) Lee, H. S.; Kim, M. S.; Jin, Y.; Han, G. H.; Lee, Y. H.; Kim, J. Efficient Exciton-Plasmon Conversion in Ag Nanowire/Monolayer MoS_2 Hybrids: Direct Imaging and Quantitative Estimation of

DOI: 10.1021/acsnano.6b03414
ACS Nano XXXX, XXX, XXX−XXX

Plasmon Coupling and Propagation. *Adv. Opt. Mater.* **2015**, *3*, 943−947.
(82) Liu, W.; Lee, B.; Naylor, C. H.; Ee, H. S.; Park, J.; Johnson, A. T. C.; Agarwal, R. Strong Exciton-Plasmon Coupling in MoS_2 Coupled with Plasmonic Lattice. *Nano Lett.* **2016**, *16*, 1262−1269.
(83) Zhao, W.; Wang, S.; Liu, B.; Verzhbitskiy, I.; Li, S.; Giustiniano, F.; Kozawa, D.; Loh, K. P.; Matsuda, K.; Okamoto, K.; et al. Exciton-Plasmon Coupling and Electromagnetically Induced Transparency in Monolayer Semiconductors Hybridized with Ag Nanoparticles. *Adv. Mater.* **2016**, *28*, 2709−2715.
(84) Zu, S.; Li, B.; Gong, Y.; Li, Z.; Ajayan, P. M.; Fang, Z. Active Control of Plasmon-Exciton Coupling in MoS_2-Ag Hybrid Nanostructures. *Adv. Opt. Mater.* **2016**, *4*, 1463.
(85) Li, H.; Contryman, A. W.; Qian, X.; Ardakani, S. M.; Gong, Y.; Wang, X.; Weisse, J. M.; Lee, C. H.; Zhao, J.; Ajayan, P. M.; et al. Optoelectronic Crystal of Artificial Atoms in Strain-Textured Molybdenum Disulphide. *Nat. Commun.* **2015**, *6*, 7381:1−6.
(86) Michaelson, H. B. The Work Function of the Elements and Its Periodicity. *J. Appl. Phys.* **1977**, *48*, 4729−4733.
(87) Das, S.; Chen, H. Y.; Penumatcha, A. V.; Appenzeller, J. High Performance Multilayer MoS_2 Transistors with Scandium Contacts. *Nano Lett.* **2013**, *13*, 100−105.
(88) Amani, M.; Chin, M. L.; Birdwell, A. G.; O'Regan, T. P.; Najmaei, S.; Liu, Z.; Ajayan, P. M.; Lou, J.; Dubey, M. Electrical Performance of Monolayer MoS_2 Field-Effect Transistors Prepared by Chemical Vapor Deposition. *Appl. Phys. Lett.* **2013**, *102*, 193107.
(89) Ayari, A.; Cobas, E.; Ogundadegbe, O.; Fuhrer, M. S. Realization and Electrical Characterization of Ultrathin Crystals of Layered Transition-Metal Dichalcogenides. *J. Appl. Phys.* **2007**, *101*, 014507.
(90) Li, H.; Yin, Z.; He, Q.; Li, H.; Huang, X.; Lu, G.; Fam, D. W. H.; Tok, A. I. Y.; Zhang, Q.; Zhang, H. Fabrication of Single- and Multilayer MoS_2 Film-Based Field-Effect Transistors for Sensing NO at Room Temperature. *Small* **2012**, *8*, 63−67.
(91) Novoselov, K. S.; Jiang, D.; Schedin, F.; Booth, T. J.; Khotkevich, V. V.; Morozov, S. V.; Geim, A. K. Two-Dimensional Atomic Crystals. *Proc. Natl. Acad. Sci. U. S. A.* **2005**, *102*, 10451−10453.
(92) Radisavljevic, B.; Radenovic, A.; Brivio, J.; Giacometti, V.; Kis, A. Single-Layer MoS_2 Transistors. *Nat. Nanotechnol.* **2011**, *6*, 147−150.
(93) Schmidt, H.; Wang, S.; Chu, L.; Toh, M.; Kumar, R.; Zhao, W.; Neto, A. H. C.; Martin, J.; Adam, S.; Özyilmaz, B.; et al. Transport Properties of Monolayer MoS_2 Grown by Chemical Vapor Deposition. *Nano Lett.* **2014**, *14*, 1909−1913.
(94) Wu, W.; De, D.; Chang, S.-C.; Wang, Y.; Peng, H.; Bao, J.; Pei, S.-S. High Mobility and High On/Off Ratio Field-Effect Transistors Based on Chemical Vapor Deposited Single-Crystal MoS_2 Grains. *Appl. Phys. Lett.* **2013**, *102*, 142106.
(95) Ceballos, F.; Bellus, M. Z.; Chiu, H.-Y.; Zhao, H. Ultrafast Charge Separation and Indirect Exciton Formation in MoS_2-$MoSe_2$ van der Waals Heterostructure. *ACS Nano* **2014**, *8*, 12717−12724.
(96) Deng, Y.; Luo, Z.; Conrad, N. J.; Liu, H.; Gong, Y.; Najmaei, S.; Ajayan, P. M.; Lou, J.; Xu, X.; Ye, P. D. Black Phosphorous-Monolayer MoS_2 van der Waals Heterojunction p-n Diode. *ACS Nano* **2014**, *8*, 8292−8299.
(97) Furchi, M. M.; Pospischil, A.; Libisch, F.; Burgdörfer, J.; Mueller, T. Photovoltaic Effect in an Electrically Tunable van der Waals Heterojunction. *Nano Lett.* **2014**, *14*, 4785−4791.
(98) Huang, L.; Huo, N.; Li, Y.; Chen, H.; Yang, J.; Wei, Z.; Li, J.; Li, S. S. Electric-Field Tunable Band Offsets in Black Phosphorus and MoS_2 van der Waals p-n Heterostructure. *J. Phys. Chem. Lett.* **2015**, *6*, 2483−2488.
(99) Lee, C. H.; Lee, G. H.; van der Zande, A. M.; Chen, W.; Li, Y.; Han, M.; Cui, X.; Arefe, G.; Nuckolls, C.; Heinz, T. F.; et al. Atomically Thin p-n Junctions with van der Waals Heterointerfaces. *Nat. Nanotechnol.* **2014**, *9*, 676−681.
(100) Yuan, J.; Najmaei, S.; Zhang, Z.; Zhang, J.; Lei, S.; Ajayan, P. M.; Yakobson, B. I.; Lou, J. Photoluminesccence Quenching and Charge Transfer in Artificial Heterostacks of Monolayer Transition Metal Dichalcogenides and Few-Layer Black Phosphorous. *ACS Nano* **2015**, *9*, 555−563.
(101) Zeng, Z.; Yin, Z.; Huang, X.; Li, H.; He, Q.; Lu, G.; Boey, F.; Zhang, H. Single-Layer Semiconducting Nanosheets: High-Yield Preparation and Device Fabrication. *Angew. Chem., Int. Ed.* **2011**, *50*, 11093−11097.
(102) Gan, L. Y.; Zhang, Q.; Cheng, Y.; Schwingenschlögl, U. Photovoltaic Heterojunctions of Fullerenes with MoS_2 and WS_2 Monolayers. *J. Phys. Chem. Lett.* **2014**, *5*, 1445−1449.
(103) Shanmugam, M.; Durcan, C. A.; Yu, B. Layered Semiconductor Molybdenum Disulfide Nanomembrane Based Schottky-Barrier Solar Cells. *Nanoscale* **2012**, *4*, 7399−7405.
(104) Scharber, M. C.; Mühlbacher, D.; Koppe, M.; Denk, P.; Waldauf, C.; Heeger, A. J.; Brabec, C. J. Design Rules for Donors in Bulk-Heterojunction Solar Cells - Towards 10% Energy-Conversion Efficiency. *Adv. Mater.* **2006**, *18*, 789−794.
(105) Waldauf, C.; Schilinsky, P.; Hauch, J.; Brabec, C. J. Material and Device Concepts for Organic Photovoltaics: Towards Competitive Efficiencies. *Thin Solid Films* **2004**, *451*−*452*, 503−507.
(106) *FDTD Solutions*; Lumerical Solutions, Inc., 2015.

DOI: 10.1021/acsnano.6b03414
ACS Nano XXXX, XXX, XXX−XXX